Spatially resolved sensitivity of single-particle plasmon sensors

THE JOURNAL OF PHYSICAL CHEMISTRY C

Article

Cite This: J. Phys. Chem. C 2018, 122, 4615−4621

pubs.acs.org/JPCC

Spatially Resolved Sensitivity of Single-Particle Plasmon Sensors

Michael A. Beuwer, Bas van Hoof, and Peter Zijlstra*

Molecular Biosensing for Medical Diagnostics, Faculty of Applied Physics and Institute for Complex Molecular Systems, Eindhoven University of Technology, PO Box 513, 5600 MB, Eindhoven, The Netherlands

Supporting Information

ABSTRACT: The high sensitivity of localized surface plasmon resonance sensors to the local refractive index allows for the detection of single-molecule binding events. Though binding events of single objects can be detected by their induced plasmon shift, the broad distribution of observed shifts remains poorly understood. Here, we perform a single-particle study wherein single nanospheres bind to a gold nanorod, and relate the observed plasmon shift to the binding location using correlative microscopy. To achieve this we combine atomic force microscopy to determine the binding location, and single-particle spectroscopy to determine the corresponding plasmon shift. As expected, we find a larger plasmon shift for nanospheres binding at the tip of a rod compared to its sides, in good agreement with numerical calculations. However, we also find a broad distribution of shifts even for spheres that were bound at a similar location to the nanorod. Our correlative approach allows us to disentangle effects of nanoparticle dimensions and binding location, and by comparison to numerical calculations we find that the biggest contributor to this observed spread is the dispersion in nanosphere diameter. These experiments provide insight into the spatial sensitivity and signal-heterogeneity of single-particle plasmon sensors and provides a framework for signal interpretation in sensing applications.

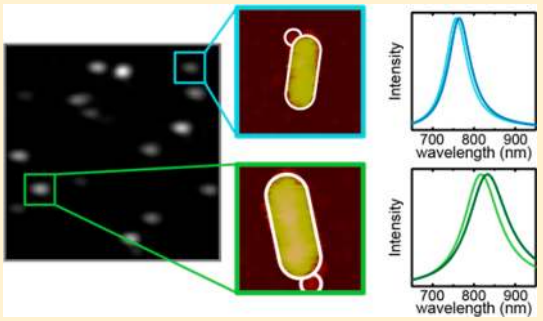

1. INTRODUCTION

Noble metal nanoparticles are ideal tools for label-free sensing.[1] When metal nanoparticles are excited with a frequency matching the collective resonance of conduction electrons this gives rise to strong scattering and absorption.[1,2] The frequency of this localized surface plasmon resonance depends on the material, shape, size, and the refractive index of the environment of the particle.[2] In the latter mechanism the particle can act as a sensor for, e.g., molecular binding events that locally change the refractive index resulting in a shift of the resonance frequency. The exquisite sensitivity allows for single-molecule detection, allowing for the detection of statistical distributions of molecular properties and rare events or molecular configurations.[3,4] Labeling of the analyte is not required, as opposed to single-molecule fluorescence techniques,[5] eliminating possible alteration of molecular behavior due to fluorescence labeling.[6] Importantly, blinking and bleaching are absent because the particle's plasmon is photostable.

Label-free detection of molecular interaction kinetics has been successfully demonstrated using plasmonic nanoparticles,[7−13] but the magnitude of the plasmon shift is not easily translated to the number of analytes bound because the shift of the plasmon resonance depends on the location at which the analyte binds.[14,15] This resonance shift scales with the overlap integral between the analyte and the locally enhanced field, so the inhomogeneity in the locally enhanced field causes a distribution of plasmon shifts depending on the binding location.[16] Moreover, the probability of analyte binding depends on particle geometry and is typically higher at protrusions due to better fluid accessibility, where the local field enhancement is also maximized.[15] It is therefore important to understand the dependence of the plasmon shift on binding location to correctly interpret sensor response and convert the signal to an analyte concentration.[14,15]

To measure both binding location and plasmon shift a correlative approach has been adopted in literature, where the plasmon shift is correlated to atomic force microscopy (AFM) or scanning electron images (SEM) of metallic nanoparticles. The plasmon response of gold colloids binding to a gold crescent-shaped nanoparticle was mapped by positioning the gold colloid near the nanocrescent tip, showing large shifts correspond to high local near-fields.[19] For triangular gold nanoplates it was shown that for anti-IgG the plasmon shift was more than twice as high when binding to the nanoplate edges compared to the flat terrace.[20] Correlated SEM and optical measurements on gold spheres bound to gold nanoplates were also combined with numerical calculations to show how heterogeneity in the constructs influences the spectral response and revealed nanoparticle size to be the dominant variable.[21] Sannomiya et al. demonstrated excellent agreement between experiment and theory for single 20 nm DNA-labeled gold nanospheres binding to 100 nm spheres.[22] Finally, Garai et al. studied the polarization dependence of the two-photon

Received: January 25, 2018
Revised: February 12, 2018
Published: February 12, 2018

DOI: 10.1021/acs.jpcc.8b00849
J. Phys. Chem. C 2018, 122, 4615−4621

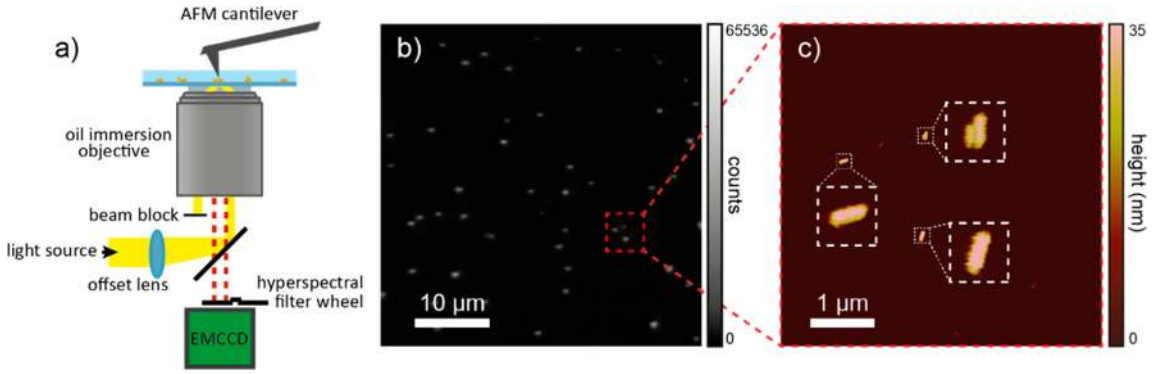

Figure 1. Experimental setup. (a) Combined AFM and total internal reflection scattering microscopy setup. The light beam was focused at the periphery of the back-aperture which results in total internal reflection from the glass−water interface. A beam block in the detection path prevents the reflected light from reaching the detector. The scattered light from the gold nanoparticles is collected by an oil immersed objective and imaged on an EMCCD camera. The sample is accessible from the top for AFM measurements. (b) Wide-field image of the scattered intensity of gold nanorods immobilized on the coverslip surface. (c) The indicated 5 × 5 μm^2 area in part b was imaged with the AFM showing the diffraction-limited spots correspond to two single nanorods and a nanorod dimer.

photoluminescence to distinguish between gold nanospheres bound to the side and the tip of a nanorod.[23]

Beyond nanoplates and nanospheres, gold nanorods have emerged as a promising geometry for plasmon sensing due to their high sensitivity to local refractive index[24] and reproducible bulk synthesis.[25] Particularly colloidal gold nanorods are attractive because their single-crystalline structure[25,26] minimizes plasmon dephasing by electron scattering, resulting in a narrow and bright longitudinal plasmon resonance.[27] Gold nanorods have been employed for detection of streptavidin,[8,9,28] antibodies,[10,11,29,30] fibronectin,[12,28] and thrombin,[28] where both ensemble-averaged[8,9,28−30] and single-molecule detection[10,12,11] have been demonstrated. For gold nanorods the location-dependent plasmon shift has been mapped on ensembles of polycrystalline particles using polymer masks covering either the particle's tip or center region[31] and for 20 nm SiO_2 dots embedded in a polymer film.[32] The highest plasmon shift was found for structures fabricated at the nanorod tip, in agreement with numerical calculations.[32] However, these were ensemble studies requiring averaging over hundreds of particles to mitigate variations due to differences in particle geometry.[31,32] Such ensemble-averaging masks particle-to-particle variations and heterogeneity, which are important contributors to the expected spread in plasmon shift.

Here, we perform a single-particle study in which we elucidate the spatial sensitivity of single-crystal gold nanorods to the binding of a model analyte (small gold spheres). Using a correlative approach combining optical and atomic force microscopy we map the position-dependent plasmon shift of single gold nanorods in response to binding of small gold nanospheres. We find that the shift of the longitudinal surface plasmon increases when the gold nanosphere binds closer to the tip of the gold nanoparticle, in excellent agreement with the numerical calculations. Because we probe single particles instead of ensembles we gain direct access to heterogeneity in the magnitude of the plasmon shift. We find that the spread in plasmon shift is not dominated by the volume or aspect ratio of the nanorods, but rather by the size-dispersion of the gold spheres. These results imply that this correlated technique is well suited to study location-dependent sensor response to, e.g., optimize site-specific functionalization protocols[17] and study location-dependent kinetics.[15]

2. EXPERIMENTAL AND THEORETICAL METHODS

2.1. Experimental Setup. We used a combined AFM and total internal reflection scattering microscopy setup (Figure 1). The excitation beam was focused on the periphery of the back-focal plane and was totally internally reflected at the glass−water interface. The reflected beam was blocked in the detection path by a half-moon shaped beamblock. The scattered signal was collected by the 100 × 1.49 NA oil immersion objective and imaged on an electron multiplying charged coupled (EMCCD) device (Andor iXon Ultra, Andor Technology Ltd., Northern Ireland). Onto the Nikon Eclipse Ti microscope an AFM stage (Bruker Bioscope Catalyst in peak-force tapping mode) was mounted to enable topographic imaging. ScanAsyst-Air cantilevers were used with a stiffness k of 0.7 N/m and a force of 2 nN was applied. AFM imaging was performed in air after rinsing and drying the sample to reveal the binding location of the gold nanosphere. In Figure 1b a typical scattering image of immobilized gold nanorods is shown with the corresponding AFM image of the indicated 5 × 5 μm^2 area shown in Figure 1c. The insets show zooms of the particles where we observe two individual nanorods and a nanorod dimer.

Spectra of single gold nanorods were recorded with hyperspectral microscopy. Using white light illumination with a broadband tungsten-halogen light source (Thorlabs, New Jersey, USA) a series of bandpass filters (10 nm full width at half-maximum and center wavelength ranging from 670 to 890 nm) was inserted into the detection path and images were recorded with an EMCCD camera. For each wavelength channel the scattered intensity was determined by fitting the diffraction limited spots with a 2D Gaussian and correcting for the spectral profile of the light source. The plasmon resonance wavelength and line width were then determined by fitting a Lorentzian function to the scattering intensity as a function of photon energy for each nanoparticle.

Spectra were recorded for all nanorods, where particles with spectra with a broadened line width, i.e., more than two times the standard deviation, or with a non-Lorentzian-shape were discarded as clusters. The variation in scattering intensity we observe in the wide-field images is due to size dispersion (see Figure S1 in the Supporting Information) and particle orientation with respect to the partially polarized evanescent field. In Figure S3 of the Supporting Information the

DOI: 10.1021/acs.jpcc.8b00849
J. Phys. Chem. C 2018, 122, 4615−4621

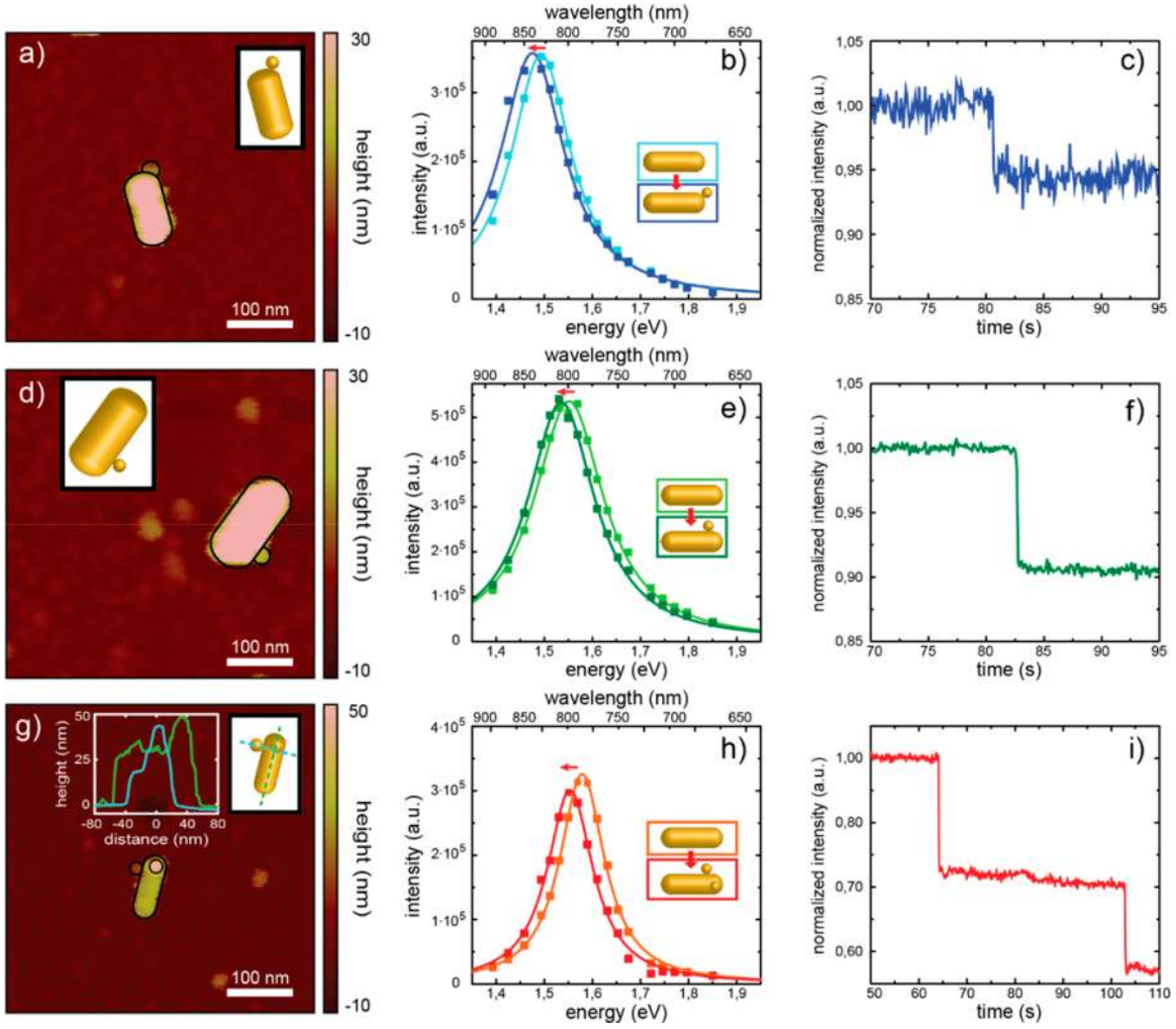

Figure 2. Correlated atomic force microscopy and microsphere binding to individual gold nanorods. From AFM images (a, d, g) the binding position is determined. Insets show the binding position of the nanospheres to the nanorods. In the inset in part g, cross sections along the longitudinal and transversal axis of the nanorod show the dimensions of the gold nanoparticles. The total plasmon shift is extracted from the scattering spectra before and after incubation in gold nanospheres (b, e, h). Monitoring the scattering intensity in time at a single excitation wavelength results in stepwise changes in scattered intensity due to nanosphere binding (c, f, i). On some particles, we observe multiple binding events evidenced by multiple stepwise intensity changes (i).

distribution of LSPR wavelengths, line width and plasmon shift for all particles in a typical field of view is shown. Gaussian fits to these distributions give an average LSPR wavelength of 793 ± 38 nm and a line width of 157 ± 20 meV, corresponding excellently to the numerically calculated values for a 120 nm by 40 nm gold nanorod in water on a glass surface.

Real-time measurements of single 20 nm gold nanospheres binding to the immobilized gold nanorods were performed by illuminating with a fiber-coupled light emitting diode (Thorlabs, New Jersey, USA) with a center wavelength of 780 nm and a line width of 29 nm. A shift in the nanorod spectra due to a nanosphere binding event causes an intensity change, where each step in the signal corresponds to a single binding event. The step is positive or negative depending on the LSPR wavelength of the nanorod with respect to the probe excitation spectrum. These time traces were used to identify particles that exhibited one or more binding events, while the magnitude of the plasmon shift was extracted from the scattering spectra before and after binding.

2.2. Sample Preparation. Samples were prepared by spin coating 40 × 120 nm^2 gold nanorods (Nanoseedz, Hong Kong) at 2000 rpm for 2 min onto glass coverslips. Before spin-coating the glass coverslips were sonicated in methanol and UV/ozone-cleaned for 90 min. After spin coating the samples were rinsed with methanol, PBS and water and blown dry under N_2-flow.

To induce gold nanospheres binding to the gold nanorods we used cysteine-cysteine coupling.[23] Cysteine binds covalently to the particles via a gold−thiol interaction. Coupling of spheres to rods was achieved at a pH of 2.3 at which cysteine is zwitterionic and allows for nanosphere-nanorod coupling by electrostatic interactions.[23] The immobilized gold nanorods were first incubated in 100 μM L-cysteine (Sigma-Aldrich) in pH 2.3 Milli-Q water. A solution containing 1.2 nM of 20 nm gold nanospheres (Sigma-Aldrich) was then flown in and incubated for 30 min while a time-trace was recorded. Afterward the sample was flushed with MQ water adjusted to pH 2.3 to wash away unbound gold nanospheres and cysteine. On the basis of the dimensions of two bound cysteine molecules an interparticle spacing of ∼1 nm is assumed.[23]

DOI: 10.1021/acs.jpcc.8b00849
J. Phys. Chem. C 2018, 122, 4615−4621

3. RESULTS AND DISCUSSION

The results for three typical nanoparticles are shown in Figure 2. The AFM scans show different heterodimer configurations where the nanorods in Figure 2, parts a and d, have bound a single gold nanosphere, whereas in Figure 2g we observe two bound nanospheres. The corresponding plasmon shifts, as measured from the Lorentzian fit to the spectra, are 10.3 nm (Figure 2b), 8.3 nm (Figure 2e), and 12.7 nm (Figure 2h). The time-traces recorded on the same particles confirm this behavior as the number of observed stepwise changes in intensity matches the number of bound spheres. For approximately 15% of the particles stepwise changes were observed in the scattering intensity time-traces, indicating one or more gold nanosphere binding events.

In Figure 3 the distribution of measured plasmon shifts is shown for nanorods with zero, one and two nanoparticles bound. For particles that show no binding events we find an average plasmon shift of 2.1 ± 1.3 nm, which we attribute to additional cysteine binding to the gold nanorods in the time that passes between the acquisition of both scattering spectra. To gain more insight in the distribution of shifts we performed boundary element method (BEM) calculations.[33] The gold nanorod is modeled as a 120 nm long and 40 nm wide spherically capped cylinder, the dimensions as determined from TEM images (Figure S1 in the Supporting Information). The modeled nanosphere has a diameter of 20 nm and was placed at a distance of 1 nm from the gold nanorod corresponding to the length of a cysteine dimer.[23] Calculations were performed for the gold nanorod in water positioned 0.3 nm above a glass substrate.[34] The measured distribution shown in Figure 3 is in good agreement with the BEM simulations (Figure S6 in the Supporting Information), where we also observe a broad range of shifts up to 15 nm. The largest observed shifts corresponds to nanospheres binding at the tip of the nanorod. In both experiments and theory, we observe an increased probability of small plasmon shifts, which we attribute to the relatively large surface area of the side-faces of the particles.

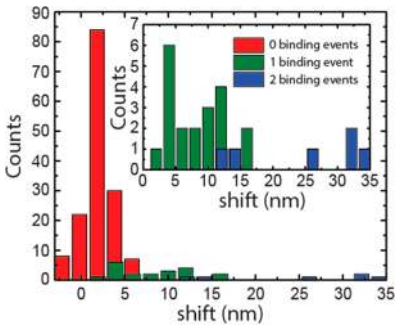

Figure 3. Measured distribution of end-point plasmon shifts due to nanosphere binding. The total number of binding events for each particle was determined by counting stepwise intensity changes in the time traces. A Gaussian fit to the distribution of plasmon shifts for zero binding events yields a shift of 2.1 ± 1.2 nm, caused cysteine molecules binding during incubation. In the inset a zoom of the distributions of one and two binding events are shown.

Both the measured and calculated distribution of shifts show a broad spread, in the next discussion we investigate the origin of this spread. In parts a and b of Figure 4, the electric field amplitude normalized to the incoming field is shown for two heterodimer configurations. The excitation of the longitudinal plasmon in combination with the lightning rod effect results in strong local fields at the nanorod tip compared to the nanorod side. The plasmon shift depends on the overlap integral of the local field and the particle,[35] resulting in larger shifts near the tip. The electric field strength in the gap of the coupled nanosphere and nanorod is also increased at the tip (~270× enhancement) compared to the side (~30× enhancement). In Figure 4c, the calculated plasmon shift is shown for 11 different binding locations at interparticle distances varying from 1−10 nm. Because of the rapidly decaying enhanced field the plasmon shift decreases strongly with distance. This illustrates the importance of thin coatings and small capture molecules on nanoparticle sensors to optimize the shift induced by molecular binding. The plasmon shift strongly decreases as the nanosphere is moved from the tip to the side of the nanorod because of the decreasing near-field intensity. Interesting to note is the influence of the presence of the substrate on the position-dependent plasmon shift. Position "9" and position "11" are identical in the absence of the substrate due to rotational symmetry, but in the presence of the substrate we find a ~ 10%

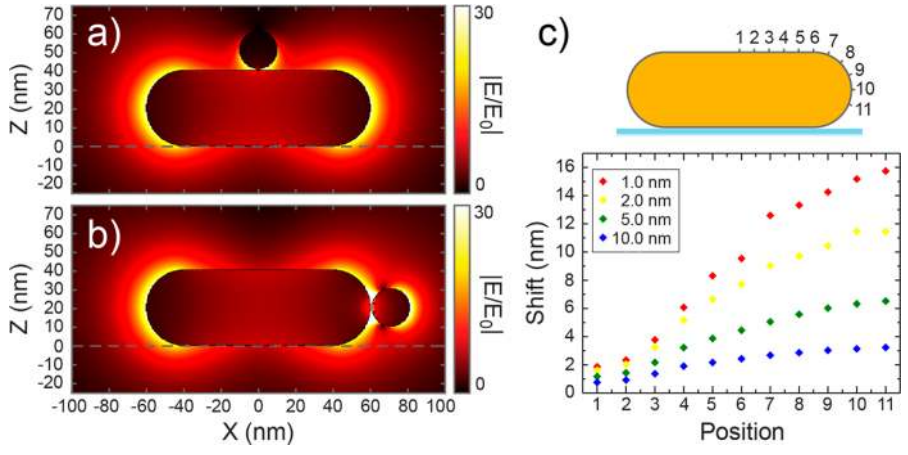

Figure 4. BEM simulations of local electric field enhancement and plasmon shift. Calculated normalized electric field $|E/E_0|$ around a gold heterodimer with a gold nanosphere at the side (a) and at the tip (b). Fields are calculated for a polarization along the long axes and a wavelength resonant with the longitudinal plasmon resonance wavelength of the dimer. (c) Plasmon shift as a function of binding position for a 20 nm sphere near a 40 × 120 nm^2 gold nanorod on a glass substrate for interparticle distances from 1−10 nm.

DOI: 10.1021/acs.jpcc.8b00849
J. Phys. Chem. C 2018, 122, 4615−4621

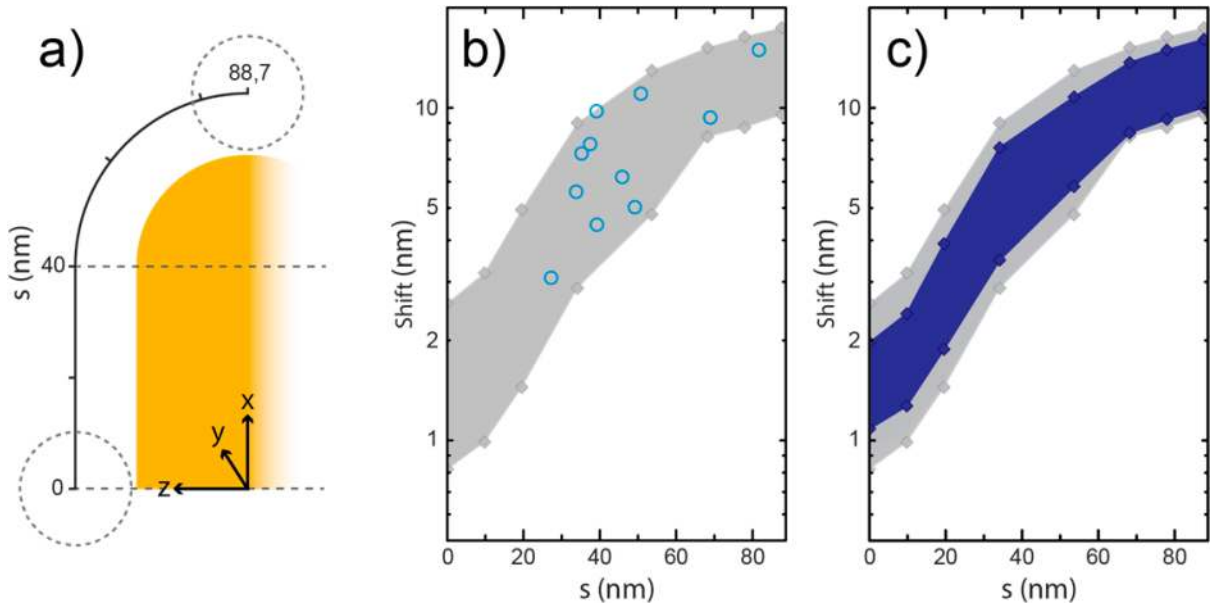

Figure 5. (a) Binding position along the nanorod s for a 40 nm wide and 120 nm long nanorod. The gray dashed circles in the cartoon show the binding position of the gold nanospheres at the side (s = 0 nm) and tip (s = 88.7 nm). (b) Measured plasmon shifts of single nanosphere binding events as a function of the coordinate s as measured by AFM (blue open circles). The light gray area indicates the range of shifts (standard deviation) based on the distribution of nanorod and nanosphere dimensions present in the samples, where the gray diamonds are the calculated values for different binding positions along the nanorod. (c) Calculated distribution of plasmon shift due to dispersion of nanosphere diameter (blue shaded area and blue diamonds) and the total distribution of shift due to the distribution of both nanorod and nanosphere dimensions. Deviations from a smooth curve are due to the finite mesh size used in the numerical calculations.

larger plasmon shift at position "11" due to the slightly enhanced field in the gap region between the tip of the particle and the glass substrate.

From the correlated images shown in Figure 2, we extract the binding location and plasmon shift, the results of this correlation are shown in Figure 5 (blue open circles). The binding location s is represented as the coordinate along the gold nanorod surface, starting from the center of the side facet. When nanospheres are bound outside the XZ-plane the 3D-position was projected onto the XZ-plane. This is possible because of the radial symmetry of the nanorod if we neglect the presence of the substrate. In doing so we introduce an estimated uncertainty of ~10% in the expected plasmon shift (see Figure 4c), which is significantly less than the heterogeneity we observe in Figure 5. To aggregate and compare binding positions for particles with slightly different dimensions we rescale s to a 120 nm × 40 nm gold nanorod. This will introduce a small uncertainty in the position-determination, which we estimate to be less than 2 nm based on BEM simulations with different nanorod volume and aspect ratio, again much smaller than the observed heterogeneity. For side-bound nanospheres the error in shift is even less than 0.5 nm. From Figure 4, we expect that tip-bound nanospheres result in plasmon shifts approximately 8× larger than side-bound nanospheres. In Figure 5a, we see the same trend, where the plasmon shift increases for gold nanospheres binding closer to the nanorod tip as expected from the numerical simulations. Side-bound spheres induce a small but nonzero shift that is caused by the residual field-enhancement present at the side-facets of the rod; see Figure 4. We notably observe a large spread in the measured plasmon shifts with variations of nearly a factor two even for spheres bound at a similar location on the nanorod, e.g. for particles bound around s = 40 nm.

We now analyze the origin of this spread for which we calculate the expected distribution of plasmon shifts due to the distribution of nanorod and nanosphere dimensions present in the sample. These size-distributions are obtained from TEM images (see Supporting Information) that reveal a certain spread (mean ± standard deviation) in nanorod volume and aspect ratio, and in nanosphere diameter. We then performed BEM simulations for gold nanospheres bound at 10 positions along the gold nanorod at an interparticle distance of 1 nm. We repeated this for different combinations of nanorod and nanosphere dimensions, and nanorod volume, respectively. This defines the lower and upper bounds for the position-dependent plasmon shift, illustrated by the gray shaded area in Figure 5b. A more detailed explanation of the procedure can be found in the Supporting Information.

We find that nearly all measurements fall within the calculated range of plasmon shifts. In Figure 5c, we plot the contribution in the spread of plasmon shifts caused by only the dispersion in nanosphere diameter as the blue shaded area. These simulations reveal that the 10% size-dispersion in nanosphere diameter (18.1 ± 2.1 nm) dominates the observed spread in plasmon shift, whereas the distribution of nanorod volume and aspect ratio contribute significantly less to the distribution of sifts. Interestingly, the distribution of shifts for tip-bound spheres is nearly entirely determined by the distribution of sphere diameters, whereas for side-bound spheres the contribution of nanorod volumes increases. We attribute this effect to the volume-dependence of the near-field intensity (see Figure S5 in the Supporting Information). BEM calculations show that the near-field intensity around the particle decreases with increasing nanorod volume due to radiation damping.[36] This reduction is stronger at the side facets of the particle than around the tips, resulting in a larger relative contribution to the spread in plasmon shift for side-

DOI: 10.1021/acs.jpcc.8b00849
J. Phys. Chem. C 2018, 122, 4615−4621

binding (see Figure S5 in the Supporting Information). We note that variations in interparticle distance are not taken into account, however previous EM images of cysteine-coupled gold nanorod−gold nanosphere heterodimers showed a 1 nm interparticle distance estimate to be reliable.[23]

In recent single-molecule plasmon sensing studies, we[11] and others[12] reported plasmon shifts induced by single proteins to vary widely from binding event to binding event. The origin of the observed spread in molecular sensing experiments remains poorly understood but is critical for the correct interpretation of sensor response. A correlated approach such as the one presented here may be used to directly image the binding position of bound proteins to gain insight into the origins of the spread in plasmon shifts, and provide guidelines on how to minimize this heterogeneity. Although globular proteins show very little size dispersion compared to the nanospheres used here, many proteins (e.g., antibodies[11] and fibronection[12]) are not globular and thus the plasmon shift will also depend on their orientation with respect to the nanorod.

Not only the plasmon shift is spatially dependent, numerical calculations have recently shown that the binding rate is also spatially heterogeneous for diffusion-limited reactions. The binding rate at protrusions and tips is higher than near the coverslip surface due to fluid accessibility, and this heterogeneity becomes more pronounced for sharper tips and higher aspect ratios.[15] For the nanorods used in our experiments, the binding probability is predicted to be ∼25% higher at the nanorod tip compared to the side.[15] This means that knowledge of the binding location is not only required to interpret the amplitude of a sensor signal, but also to determine the kinetic constants of the biomolecular interaction.

In practical sensing implementations it is not feasible to measure the binding location of each detected protein. In contrast, site-specific functionalization protocols may be advantageous to functionalize specific regions on the particle where the sensitivity to binding is maximized.[17,18] Qualitative measurements of their efficacy have been performed,[17] but the quantitative effect on the heterogeneity in signal amplitude and kinetics is unknown. A correlated approach such as the one presented here may shed light on the origins of observed heterogeneity to allow for the tailored design and optimization of single-molecule sensors.

4. CONCLUSIONS

We have employed correlative microscopy to correlate the plasmon shift to binding position and demonstrated this for the first time on single gold nanorods. We have shown that the measured plasmon shifts fall within the expected range calculated from BEM simulations. The dominant contributor to the spread in plasmon shifts is the dispersion in size of the gold nanospheres, in combination with smaller contributions of dispersion in nanorod volume and aspect ratio. In the future correlated microscopy can be applied to evaluate efficacy of site-specific functionalization protocols, which will contribute to the improvement of single-molecule sensors.

■ ASSOCIATED CONTENT

Supporting Information

The Supporting Information is available free of charge on the ACS Publications website at DOI: 10.1021/acs.jpcc.8b00849.

Alignment procedure of AFM and dark-field microscope, size distributions of gold nanorod and nanospheres, distributions of localized surface plasmon resonance wavelength and shift, and a thorough explanation of performed BEM simulations (PDF)

■ AUTHOR INFORMATION

Corresponding Author

*(P.Z.) E-mail: p.zijlstra@tue.nl. Telephone: +31 (0)40 247 2807.

ORCID

Peter Zijlstra: 0000-0001-9804-2265

Notes

The authors declare no competing financial interest.

■ ACKNOWLEDGMENTS

We thank Marcel Verheijen for performing all TEM measurements and acknowledge Solliance and the Dutch province of Noord Brabant for funding the TEM facility. P.Z. acknowledges financial support from The Netherlands Organization for Scientific Research (NWO VIDI).

■ REFERENCES

(1) Taylor, A. B.; Zijlstra, P. Single-molecule plasmon sensing: current status and future prospects. *ACS Sens.* **2017**, *2*, 1103−1122.

(2) Zijlstra, P.; Orrit, M. Single metal nanoparticles: optical detection, spectroscopy and applications. *Rep. Prog. Phys.* **2011**, *74*, 106401.

(3) Wei, R.; Gatterdam, V.; Wieneke, R.; Tampé, R.; Rant, U. Stochastic sensing of proteins with receptor-modified solid-state nanopores. *Nat. Nanotechnol.* **2012**, *7*, 257−263.

(4) Janssen, K.; de Cremer, G.; Neely, R. K.; Kubarev, A. V.; van Loon, J.; Martens, J. A.; de Vos, D. E.; Roeffaers, M. B. J.; Hofkens, J. Single molecule methods for the study of catalysis: from enzymes to heterogeneous catalysts. *Chem. Soc. Rev.* **2014**, *43*, 990−1006.

(5) Ma, F.; Li, Y.; Tang, B.; Zhang, C. Y. Fluorescent biosensors based on single-molecule counting. *Acc. Chem. Res.* **2016**, *49*, 1722−1730.

(6) Yin, L.; Wang, W.; Wang, S.; Zhang, F.; Zhang, S.; Tao, N. How does fluorescent labeling affect the binding kinetics of proteins with intact cells? *Biosens. Biosens. Bioelectron.* **2015**, *66*, 412−416.

(7) McFarland, A. D.; van Duyne, R. P. Single silver nanoparticles a real-time optical sensors with zeptomole sensitivity. *Nano Lett.* **2003**, *3*, 1057−1062.

(8) Raschke, G.; Kowarik, S.; Franzl, T.; Sönnichsen, C.; Klar, T. A.; Feldmann, J.; et al. Biomolecular recognition based on single gold nanoparticle light scattering. *Nano Lett.* **2003**, *3*, 935−938.

(9) Nusz, G. J.; Marinakos, S. M.; Curry, A. C.; Dahlin, A.; Höök, F.; Wax, A.; Chilkoti, A. Label-free plasmonic detection of biomolecular binding by a single gold nanorod. *Anal. Chem.* **2008**, *80*, 984−989.

(10) Zijlstra, P.; Paulo, P. M. R.; Orrit, M. Optical detection of single non-absorbing molecules using the surface plasmon resonance of a gold nanorod. *Nat. Nanotechnol.* **2012**, *7*, 379−381.

(11) Beuwer, M. A.; Prins, M. W. J.; Zijlstra, P. Stochastic protein interactions monitored by hundreds of single-molecule plasmonic biosensors. *Nano Lett.* **2015**, *15*, 3507−3511.

(12) Ament, I.; Prasad, J.; Henkel, A.; Schmachtel, S.; Sönnichsen, C. Single unlabeled protein detection on individual plasmonic nanoparticles. *Nano Lett.* **2012**, *12*, 1092−1095.

(13) Gooding, J. J.; Gaus, K. Single-molecule sensors: challenges and opportunities for quantitative analysis. *Angew. Chem., Int. Ed.* **2016**, *55*, 11354−11366.

(14) Claudio, V.; Dahlin, A. B.; Antosiewicz, T. J. Single-particle plasmon sensing of discrete molecular events: binding position versus signal variations for different sensor geometries. *J. Phys. Chem. C* **2014**, *118*, 6980−6988.

(15) Antosiewicz, T. J.; Käll, M. A multiscale approach to modeling plasmonic nanorod biosensors. *J. Phys. Chem. C* **2016**, *120*, 20692−20701.

(16) Krug, M. K.; Schaffernak, G.; Belitsch, M.; Gašparić, M.; Leitgeb, V.; Trügler, A.; Hohenester, U.; Krenn, J. R.; Hohenau, A. Mapping the local particle plasmon sensitivity with a scanning probe. *Nanoscale* **2016**, *8*, 16449−16454.
(17) Zijlstra, P.; Paulo, P. M. R.; Yu, K.; Xu, Q.-H.; Orrit, M. Chemical interface damping in single gold nanorods and its near elimination by tip-specific functionalization. *Angew. Chem., Int. Ed.* **2012**, *51*, 8352−8355.
(18) Paulo, P. M. R.; Zijlstra, P.; Orrit, M.; Garcia-Fernandez, E.; Pace, T. C. S.; Viana, A. S.; Costa, S. M. B. Tip-specific functionalization of gold nanorods for plasmonic biosensing: effect of linker chain length. *Langmuir* **2017**, *33*, 6503−6510.
(19) Unger, A.; Rietzler, U.; Berger, R.; Kreiter, M. Sensitivity of crescent-shaped metal nanoparticles to attachment of dielectric colloids. *Nano Lett.* **2009**, *9*, 2311−2315.
(20) Beeram, S. R.; Zamborini, F. P. Effect of protein binding coverage, location, and distance on the localized surface plasmon resonance response of purified Au nanoplates grown directly on surfaces. *J. Phys. Chem. C* **2011**, *115*, 7364−7371.
(21) Fang, A.; White, S. L.; Masitas, R. A.; Zamborini, F. P.; Jain, P. K. One-to-one correlation between structure and optical response in a heterogeneous distribution of plasmonic constructs. *J. Phys. Chem. C* **2015**, *119*, 24086−24094.
(22) Sannomiya, T.; Hafner, C.; Voros, J. In situ sensing of single binding events by localized surface plasmon resonance. *Nano Lett.* **2008**, *8*, 3450−3455.
(23) Garai, M.; Zhang, T.; Gao, N.; Zhu, H.; Xu, Q.-H. Single-particle studies on two-photon photoluminescence of gold nanorod-nanosphere heterodimers. *J. Phys. Chem. C* **2016**, *120*, 11621−11630.
(24) Becker, J.; Trügler, A.; Jakab, A.; Hohenester, U.; Sönnichsen, C. The optimal aspect ratio of gold nanorods for plasmonic bio-sensing. *Plasmonics* **2010**, *5*, 161−167.
(25) Nikoobakht, B.; El-Sayed, M. A. Preparation and growth mechanism of gold nanorods (NRs) using seed-mediated growth method. *Chem. Mater.* **2003**, *15*, 1957−1962.
(26) Katz-Boon, H.; Rossouw, C. J.; Weyland, M.; Funston, A. M.; Mulvaney, P.; Etheridge, J. Three-dimensional morphology and crystallography of golf nanorods. *Nano Lett.* **2011**, *11*, 273−278.
(27) Liu, M.; Guyot-Sionnest, P.; Lee, T.-W.; Gray, S. K. Optical properties of rodlike and bipyramidal gold nanoparticles from three-dimensional computations. *Phys. Rev. B: Condens. Matter Mater. Phys.* **2007**, *76*, 235428.
(28) Rosman, C.; Prasad, J.; Neiser, A.; Henkel, A.; Edgar, J.; Sönnichsen, C. Multiplexed plasmon sensor for rapid label-free analyte detection. *Nano Lett.* **2013**, *13*, 3243−3247.
(29) Mayer, K. M.; Lee, S.; Liao, H.; Rostro, B. C.; Fuentes, A.; Scully, P. T.; Nehl, C. L.; Hafner, J. H. A label-free immunoassay based upon localized surface plasmon resonance of gold nanorods. *ACS Nano* **2008**, *2*, 687−692.
(30) Lee, S.; Mayer, K. M.; Hafner, J. H. Improved localized surface plasmon resonance immunoassay with gold bipyramid substrates. *Anal. Chem.* **2009**, *81*, 4450−4455.
(31) Piliarik, M.; Kvasnička, P.; Galler, N.; Krenn, J. R.; Homola, J. Local refractive index sensitivity of plasmonic nanoparticles. *Opt. Express* **2011**, *19*, 9213−9220.
(32) Leitgeb, V.; Trügler, A.; Köstler, S.; Krug, M. H.; Hohenester, U.; Hohenau, A.; Leitner, A.; Krenn, J. R. Three dimensional sensitivity characterization of plasmonic nanorods for refractometric biosensors. *Nanoscale* **2016**, *8*, 2974−2981.
(33) Hohenester, U.; Trügler, A. MNPBEM − a Matlab toolbox for the simulation of plasmonic nanoparticles. *Comput. Phys. Commun.* **2012**, *183*, 370−381.
(34) Waxenegger, J.; Trügler, A.; Hohenester, U. Plasmonic simulations with the MNPBEM toolbox: consideration of substrates and layer structures. *Comput. Phys. Commun.* **2015**, *193*, 138−150.
(35) Yang, J.; Giessen, H.; Lalanne, P. Simple analytical expression for the peak-frequency shifts of plasmonic resonances for sensing. *Nano Lett.* **2015**, *15*, 3439−344.
(36) Sönnichsen, C.; Franzl, T.; Wilk, T.; von Plessen, G.; Feldmann, J.; et al. Drastic reduction of plasmon damping in gold nanorods. *Phys. Rev. Lett.* **2002**, *88*, 077402.

DOI: 10.1021/acs.jpcc.8b00849
J. Phys. Chem. C 2018, 122, 4615−4621